Analytical free streamline solutions for geometrical cavitation inside sharp-edged and profiled nozzles

Alvaro Pardo-Vigil,[1] José González Pérez,[1] and Adrián Pandal[1]
Fluid Mechanics Area, Energy Department, University of Oviedo, Wilfredo Ricart St., East Departmental Building, Gijón (Spain)

(*Electronic mail: pardoalvaro@uniovi.es)

(Dated: 29 June 2025)

An analytical solution for cavitation inside a contracting nozzle is obtained applying free streamline theory. The present mathematical model is derived for two different geometries, representing sharp-edged and profiled nozzle shapes. The non-dimensional cavity profile, width and length are obtained as a function of the nozzle contraction ratio and the cavitation number. In addition, ideal flow assumptions and control volume theory are applied to predict the mass flow choking characteristics of the nozzle as a function of the pressure drop. This calculation is used to successfully validate the performance of the proposed model against experimental results and Computational Fluid Dynamics (CFD) calculations, exhibiting close agreement in both cases. Pressure recovery after cavity breakup is also calculated, and cavity condensation is modeled by means of a Homogeneous Relaxation Model (HRM) coupled to the pressure profile along the free streamline, allowing to graphically represent the cavity morphology. The analytical solution being introduced is therefore aimed at providing a valuable theoretical tool for the design process of injection and atomization systems, allowing to perform a quick check on cavitation occurrence.

I. INTRODUCTION

The study of hydrodynamic cavitation from the experimental, numerical and theoretical standpoints has been the subject of considerable research efforts in the field of Fluid Mechanics[1,2]. Among the classical cavitation problems, hydraulic pumps and turbines[3], ship propellers[4] and axisymmetric headforms[5] stand out as the most widely studied. More recently, however, cavitation inside injector nozzles has attracted significant interest due to its potential benefits for spray atomization[6].

In all of the cases mentioned above, the phase change process of cavitation is known to begin in the form of heterogeneous nucleation from preexisting bubbles termed nuclei[7]. For a pure liquid in the absence of impurities and nuclei, cavitation inception would depend on homogeneous nucleation. This leads to inception pressures below -70 MPa[8] even though the thermodynamic conditions for phase change are already favorable at the vapor pressure p_V corresponding to the working temperature. However, when enough nuclei are present in the fluid, evaporation occurs at p_V. This is the case for most industrial flows in which the working fluid does not undergo a degassing or deaeration process. The differences between nuclei-abundant and nuclei-free liquids have been studied by Briançon-Marjollet, Franc, and Michel [9] or Venning, Pearce, and Brandner [10] . More recently, Brandner, Venning, and Pearce [11] showed that while viscous effects, bubble transport and boundary layer separation play a critical role in nuclei-deplete cases, pressure drop is the main governing factor in nuclei-abundant flows. In such conditions, the agreement between two-phase potential flow solutions[12] and experiments is found to be very close.

A. Nozzle cavitation

The earliest work on nozzle cavitation dates back to the mid-twentieth century, when the foundational experiments of Bergwerk [13] were conducted on diesel nozzles. Nevertheless, the interest on the topic was laid aside until the 1990s, when momentum was recovered after the promulgation of the first emissions regulations in the automotive sector. In the context of these investigations,

the modifications induced by cavitation in jet patterns and flow features were found to have both beneficial and pernicious effects.

On the one hand, in-nozzle cavitation promotes a higher atomization of the liquid being injected. In the course of the experiments by Sou, Hosokawa, and Tomiyama [14] on a two-dimensional contraction nozzle, it was found that the growth of cavities along the throat walls at low cavitation numbers gave rise to a vapor recirculation zone characterized by an unsteady re-entrant jet regime. As a result, the span of the outgoing jet benefited from a widening effect and droplets of smaller size were formed. The experimental works by Yan and Thorpe [15], He and Ruiz [16] or Kato *et al.* [17] described analogous trends, together with other phenomena such as flow choking at very low cavitation numbers or air entrainment in the cavity wake.

On the other hand, the unsteady nature of cavitation is responsible for the rise of flow instabilities that are generally undesirable and detrimental to smoothness in the operation of atomization systems. The cavity shedding induced by the re-entrant liquid flow, as described by Karathanassis *et al.* [18] and explained by Wang and Zhang [19], promotes pressure and flow rate oscillations. In its most developed stage, this regime is denoted *hydraulic flip*[14], and is characterized by and alternating growth and collapse of cavities at each side of the nozzle throat, which a periodical deflection in the outgoing jet. What is more, the collapse of cavitation bubbles near walls during condensation is responsible for increased material erosion, reducing the lifetime and reliability of injection systems. Recent studies conducted by Özgünoğlu *et al.* [20] and Wang, Cheng, and Ji [21] have shown that nozzle walls are prone to experience a loss of material in the zone closest to the cavity collapse point, compromising the structural integrity of engines and altering the injector geometry.

Two well-defined cavity morphologies are known to take place in nozzle cavitation, namely geometrical and string cavitation[22,23]. String cavitation is observed in axisymmetric nozzles, and is due to the pre-rotation induced on the inlet flow by the injector needle[24]. The mechanisms governing this type of morphology coincide with those operating for the well-known vortex rope developed in Francis runners[25]: when a swirling flow is promoted, a low-pressure vortex core is developed and cavitation takes place. In the case of geometrical cavitation, flow separation is the main factor determining its occurrence[26]. The sudden acceleration of the flow, especially at very small nozzle contraction ratios, promotes high velocities that substantially reduce the static pressure. In addition, sharp-edged geometries lead to severe *vena contracta* effects, creating a low-pressure recirculation region in which cavities grow. Geometrical cavitation is the main area of study in nozzle cavitation, as it produces flow choking resulting from the section reduction motivated by cavity growth[27]. In addition, a controlled state of geometrical cavitation has the potential to improve atomization, as well as increasing the jet opening angle at the outlet of the nozzle[14].

The prediction of cavitation occurrence in injectors (both for swirling and geometrical morphologies) is currently based on multiphase Computer Fluid Dynamics (CFD) calculations. Different modeling approaches have been followed, with variable degrees of physical accuracy and computational cost[28]. Multiscale Eulerian-Lagrangian models like the ones developed by Hsiao, Ma, and Chahine [29] or Vallier [30] switch between a homogeneous flow assumption and a Lagrangian description of single bubble dynamics. These formulations, although very accurate, have a very high computational cost. Single bubble behavior in such models is controlled by the Rayleigh-Plesset equation[31]. Conversely, homogeneous mixture models are computationally efficient and represent the most widely used solution at both the industrial and academic levels because they allow to model both dispersed bubbles and macrocavities[32], as well as offering the possibility to couple a population balance model to increase precision[33]. The phase change source terms of these models are based on a simplified version of the Rayleigh-Plesset equation, namely the Rayleigh equation[34], that neglects viscosity, surface tension and second order dynamics. The Schnerr-Sauer model[35] must be mentioned as the most popular among them due to its simplicity and numerical stability.

In spite of the existence of multiphase CFD models allowing to predict the cavitation characteristics of a nozzle during the design stage, there is an evident lack of analytical knowledge that could be helpful during the early phases of injection system design. This gap is currently filled by empirical correlations for the inception and development of cavitation[36]. However, this is not the case for similar cavitation problems such as cavitation around a sphere[12] or in a blade cascade[37], both of which have well-known analytical free streamline solutions.

B. Free streamline theory

Free streamline theory has traditionally been the best tool for the analytical study of cavitating flows, with extensive mathematical efforts being devoted to its development[38,39]. The use of these mathematical methods, however, is not restricted to cavitation. Analytical solutions for the outlet jet from an aperture[40], the flow entering a Borda mouthpiece[41], the Coandă flow past a flat plate[42], the jet flow from an orifice[41], the flow past arbitrary-shaped obstacles[43], the flow past a rotating cylinder[44] or a Joukowsky airfoil[45] have been developed, among others. Most of the aforementioned flows are either separated (obstacle, cylinder) or have a liquid-gas interface (jet, orifice, Coandă). This is due to the fact that the assumptions of potential flow neglect viscous effects, the obtained solutions being more accurate as the influence of the boundary layer is reduced.

The solution method for a free streamline problem is generally based on conformal mapping of the hodograph corresponding to the streamline of interest. Along this streamline, the velocity modulus and direction vector must be known at certain control points, and the evolution of pressure and velocity between these points is obtained as a result of the calculation. Problem closure is provided by the irrotational flow assumption, with a zero curl for the velocity field $\mathbf{V}$:

$$\nabla \times \mathbf{V} = 0 \tag{1}$$

Which, in two dimensions, implies that:

$$\frac{\partial u}{\partial y} = \frac{\partial v}{\partial x} \tag{2}$$

where u and v are, respectively, the velocity components in the x and y Cartesian coordinates. Using equation (2) and the information available at the control points of the streamline, the velocity along the streamline is first represented in complex coordinates and later mapped through conformal transformations to a more convenient domain where $\mathbf{V}$ can be integrated in space to find the coordinates (x,y) of the streamline profile.

Besides the basic potential flow assumptions described above, the theoretical background for the present work is based on the notched hodograph method proposed by Roshko [44], in which the cavity closure is modeled as a straight line (or *notch*) in the hodograph plane.

C. Overview

Attending to the theoretical knowledge gaps that have been identified along this introductory section, the present work is aimed at developing an analytical solution for geometrical cavitation in a two-dimensional nozzle. This solution, based on free streamline theory, is calculated for both sharp-edged and profiled nozzle shapes, thus allowing to study the influence of the geometry upstream the throat section. In first place, the problem statement is discussed, including all the relevant assumptions and simplifications needed to guarantee the existence of a unique solution in the sharp-edged and profiled cases. Subsequently, the mathematical development of the solution procedure is detailed (keeping the distinction between sharp-edged and profiled nozzles). This includes the definition of the complex velocity potential, the establishment of ancillary solution planes and the translation from the hodograph plane to the positive real axis through the necessary conformal mappings. Afterwards, the results arising from the application of the model are presented and discussed. The problem solution is provided in the form of graphs intended to facilitate the interpretation, as well as providing a quick design tool for industrial and academic practitioners. Special attention is paid to differences motivated by changes in the angle and shape of the nozzle wall, as well as the throat contraction ratio. The experimental work of Winklhofer *et al.* [46] is used to validate the model, whose performance is also compared with the numerical results from Payri *et al.* [47]. Finally, conclusions are drawn from the results presented, and suggestions for future works are included.

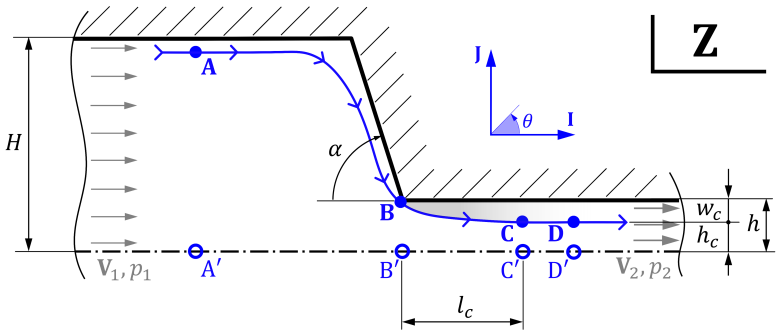

FIG. 1. Problem geometry and statement for the sharp-edged nozzle. The free streamline is depicted as a solid blue line, showing the locations of the four points of interest **A**, **B**, **C** and **D**.

II. PROBLEM STATEMENT

The first step to be undertaken in the solution process of any free streamline problem is the definition of a clear statement. In this spirit, assumptions and simplifications need to be applied in order to allow an analytical (and unique) solution of the equations. Besides the well-known simplifications inherent to potential flow such as neglecting viscous and rotational effects, additional adjustments are performed based on both elementary fluid dynamic principles or experimental evidence. Along this section, the sharp-edged and profiled nozzle cases will be separated for the sake of clarity. In any case, the flow inside the nozzle will be characterized by means of two parameters, namely the geometrical contraction ratio μ:

$$\mu = \frac{h}{H} \tag{3}$$

where h is the outlet width and H the inlet width, and the cavitation number σ:

$$\sigma = \frac{(p_2 - p_V)}{\frac{1}{2}\rho_L |\mathbf{V}_2|^2} \tag{4}$$

Where p_2 is the outlet static pressure, p_V is the vapour pressure, ρ_L is the liquid density and $|\mathbf{V}_2|$ is the outlet velocity modulus.

A. Sharp-edged nozzle

The geometrical parameters defining the problem formulation for the sharp-edged nozzle are shown in figure 1, where the walls are depicted in black solid lines, the boundary conditions are plotted in gray and the free streamline profile is represented in blue. The Cartesian two-dimensional complex plane is denoted Z, the real part corresponding to the axial (horizontal) coordinate and the imaginary part identifying the radial (vertical) coordinate. The unit vector in the axial direction is termed **I**, while the unit vector in the vertical direction is called **J** following classical notation (if the flow were axisymmetric instead of two-dimensional, this coordinate would correspond to the radial direction).

The complex velocity V_Z at each location in Z can then be expressed in complex exponential notation (using the complex conjugate):

$$V_Z = |\mathbf{V}| e^{-i\theta} \tag{5}$$

Which can easily be converted to vector notation:

$$\mathbf{V} = u\mathbf{I} - v\mathbf{J} = Re(V_Z)\mathbf{I} + Im(V_Z)\mathbf{J} \tag{6}$$

Four characteristic points **A**, **B**, **C**, **D** are identified in the free streamline, each of which must have a known velocity modulus $|\mathbf{V}|$ and argument θ:

- For point **A**, located at upstream infinity, both the modulus and argument are known. Regarding the modulus, the inlet flow has a known velocity magnitude $|\mathbf{V}_1|$. In addition, as this point is located at upstream infinity, the argument θ is trivially zero, i.e. the inlet flow is purely axial (horizontal):

$$\begin{cases} |\mathbf{V}|_A = |\mathbf{V}_1| \\ \theta_A = 0 \end{cases} \tag{7}$$

- At point **B**, located at the inlet corner of the throat section, the flow is assumed to be perfectly guided and hence the complex velocity has an argument of $-\alpha$. The velocity magnitude, however, is unknown *a priori*. Nevertheless, point **B** denotes the cavity start point and the static pressure is therefore known to be equal to p_V at the saturated liquid-vapor interface:

$$\begin{cases} |\mathbf{V}|_B = |\mathbf{V}|_{cavity} \\ \theta_B = -\alpha \end{cases} \tag{8}$$

  Hence, this information can be used in a more advanced step to find out the velocity magnitude. It shall be noted that the cavity start point may not necessarily coincide with the throat corner in a real nozzle, as the evaporation process is not instantaneous. However, experimental evidence[14] has shown that the difference between the cavity startpoint and the throat inlet is negligible from a practical standpoint.

- Point **C** is located at the cavity endpoint, where the pressure is still equal to p_V. Consequently, the velocity modulus will be the same as for **B**. Regarding the argument, the flow is considered to be perfectly aligned with the axis, meaning that:

$$\begin{cases} |\mathbf{V}|_C = |\mathbf{V}|_B = |\mathbf{V}|_{cavity} \\ \theta_C = 0 \end{cases} \tag{9}$$

- At downstream infinity, denoted by **D**, the velocity magnitude is equal to $|\mathbf{V}_2|$. Although $|\mathbf{V}_2|$ is not among the problem data, it can be deduced from continuity. However, the real outlet section of the flow is also unknown, as it is not related to the nozzle height h but to the cavity height h_c instead. Unfortunately, h_c itself is part of the solution, therefore giving rise to an implicit problem. The argument at **D** is known, as the flow is axial at downstream infinity:

$$\begin{cases} |\mathbf{V}|_D = |\mathbf{V}_2| \\ \theta_D = 0 \end{cases} \tag{10}$$

From the point-by-point analysis of the free streamline, it becomes clear that the velocity moduli at **D** and **C** (coincident with the modulus at **B**) represent the only unknowns whose value must be found before proceeding with the solution.

In first place, continuity is applied between points **A** and **D** in order to find $|\mathbf{V}_2|$. In single-phase liquid flow, the relationship between $|\mathbf{V}_1|$ and $|\mathbf{V}_2|$ is straightforward:

$$\rho_L H|\mathbf{V}_1| = \rho_L h|\mathbf{V}_2| \implies |\mathbf{V}_2| = \frac{H}{h}|\mathbf{V}_1| \tag{11}$$

However, the outlet flow is contracted due to the presence of a cavity, and the real outlet height is h_c due to flow separation. This assumption is analogous to that employed by Ambrose[48] for the calculation of head losses in miter bends, and allows to rewrite continuity for the liquid phase as:

$$|\mathbf{V}_2| = \frac{H}{h_c}|\mathbf{V}_1| \tag{12}$$

It shall be remarked that the above equation is only valid for steady flow, and assumes that flow separation remains downstream the cavity even though the static pressure has already risen above p_V. The cavity is modeled as strictly vapor-filled along its span, with the free streamline marking the liquid-vapor interface. Such assumption is common in the analytical assessment of separated flows, even in single-phase scenarios. Besides the work of Ambrose[48], this downstream persistence of flow separation was also assumed by Chu[49] or Mankbadi and Zaki[50] to solve the flow in arbitrarily turned bends, and by Smith and Duck[51] to solve the wake behind an arbitrarily shaped constriction in a closed channel. As the flow is separated in these regions, its velocity is considered negligible and the continuity equation (12) thus holds instead of (11). This assumption is essential to allow a mathematical closure of the model, as the computation of a recovery region for the initial width h after the cavity endpoint requires the definition of additional points (together with additional assumptions on the concavity of convexity of the streamline in this region) that would make the problem statement incompatible with an analytical solution by conformal mapping.

Once the magnitude of the outlet velocity has been found out, $|\mathbf{V}|_{cavity}$ at the cavity interface can be expressed as a function of $|\mathbf{V}_2|$ following Bernoulli's theorem between **C** and **D**:

$$\frac{1}{2}\rho_L|\mathbf{V}|^2_{cavity} + p_V = \frac{1}{2}\rho_L|\mathbf{V}_2|^2 + p_2 \tag{13}$$

Rearranging the terms, it is possible to relate $|\mathbf{V}|_{cavity}$ and $|\mathbf{V}_2|$ through a proportionality constant k :

$$|\mathbf{V}|_{cavity} = k|\mathbf{V}_2| \tag{14}$$

which is a function of the cavitation number:

$$\begin{gathered}|\mathbf{V}|^2_{cavity} - |\mathbf{V}_2|^2 = \frac{p_2 - p_V}{\frac{1}{2}\rho_L} \implies k^2 - 1 = \frac{p_2 - p_V}{\frac{1}{2}\rho_L|\mathbf{V}_2|^2} = \sigma \\ k = \sqrt{1+\sigma}\end{gathered} \tag{15}$$

The velocity at the cavity is therefore greater or equal than the outlet velocity, as $\sigma \geq 0$. The use of such constant k and its definition are common to free streamline problems involving cavitation (see for instance Brennen[1] or Wade[37]). Combining the above expression with the results obtained from continuity, it becomes clear that the cavity interface velocity is a function of the cavitation number σ and the flow contraction ratio μ_c, which is also a function of the geometrical contraction ratio μ and the cavitation number σ:

$$|\mathbf{V}|_{cavity} = \frac{|\mathbf{V}_1|}{\mu_c}\sqrt{1+\sigma} \tag{16}$$

With the previous results, all the information needed at the points of interest for the free streamline is available, as summarized in table I.

Finally, attention should be drawn towards the projected points **A'**, **B'**, **C'** and **D'** shown in figures 1 and 2. In these locations, the velocity is always axial and its magnitude varies from $|\mathbf{V}_1|$ to $|\mathbf{V}_2|$ following a trend that is not necessarily known, but will be given by the final solution instead.

It should be noted that the above application of Bernoulli's theorem between **C** and **D** implicitly entails the assumption of steady flow. In certain practical applications, however, the unsteady time evolution of cavity morphology may be of interest. Transient effects arising in response to disturbances or step changes (such as the injection of fuel in engines) can also be analyzed, in which case the unsteady form of the Bernoulli equation needs to be retrieved[52]:

$$\frac{\partial \varphi}{\partial \mathscr{T}} + \frac{1}{2}|\nabla\varphi|^2 = \frac{p_\infty - p_V}{\rho_L} + \frac{1}{2}|\mathbf{V}|^2_\infty \qquad \begin{cases} u = \frac{\partial \varphi}{\partial x} \\ v = \frac{\partial \varphi}{\partial y} \end{cases} \tag{17}$$

Point	Modulus, $\|\mathbf{V}\|$	Argument, θ	Pressure, p
A	$\|\mathbf{V}_2\|/\mu_c$	0	p_1
B	$k\|\mathbf{V}_2\|$	$-\alpha$	p_V
C	$k\|\mathbf{V}_2\|$	0	p_V
D	$\|\mathbf{V}_2\|$	0	p_2

TABLE I. Available information for the free streamline points in the sharp-edged nozzle.

where $\mathscr{T}$ represents time. If a far-field perturbation is imposed either on pressure or velocity (this can affect either the inlet or outlet conditions as the ∞ point can be taken both infinitely upstream or downstream the cavity), then the velocity potential φ , as defined in the *Solution Procedure* section, will evolve according to equation (17). Taking first order centered differences, a numerical solution can be achieved:

$$\varphi_{\mathscr{T}+\Delta\mathscr{T}/2} = \varphi_{\mathscr{T}-\Delta\mathscr{T}/2} + \Delta\mathscr{T}\left[\frac{p_{\infty,\mathscr{T}} - p_V}{\rho_L} + \frac{1}{2}\left(|\mathbf{V}|^2_\infty - |\nabla\varphi|^2_{\mathscr{T}}\right)\right] \tag{18}$$

If the steady flow field that is calculated in the present work is taken as the initial solution for the unsteady calculation following equation (18), then the dynamic response of cavity size and mass flow rate to pressure and velocity perturbations can be found numerically for a given $p_\infty(\mathscr{T})$ or $\mathbf{V}_\infty(\mathscr{T})$ distribution. Thermal effects can also be included through the vapor pressure, which can vary with time as $p_V(\mathscr{T})$ to account for transient heating effects (e.g., temperature increase inside a combustion chamber). Although such transient analyses would yield interesting results, the present work is focused on steady-state solutions, and therefore, equation (13) is applied.

B. Profiled nozzle

The problem statement corresponding to the profiled nozzle is analogous to that described for the sharp-edged case, and the continuity and momentum conservation equations also apply. Consequently, the difference between this problem and that of sharp-edged nozzle is not related to the information at the points **A**, **B**, **C** or **D**, all of which are depicted in figure 2. Attending to this schematic, it is clear that the approximation path of the streamline towards point **B** is smoother for the profiled nozzle, even though the final angle α is the same. In the light of the above, the values in table I are also true for the profiled nozzle case. The solution procedure, however, will present substantial differences.

III. SOLUTION PROCEDURE

The solution procedure of every free streamline problem comprises three well-defined steps, namely: the definition of a hodograph plane, the conformal mapping from this plane to the complex velocity potential and the integration of the complex velocity potential to obtain the streamline profile in the Cartesian plane. The last step is in fact the one conditioning the whole derivation process, as it defines the ancillary plane on which the hodograph needs to be projected. The complex potential is defined as:

$$w = \varphi + i\psi \tag{19}$$

where the real part φ is called *velocity potential* and the imaginary part ψ is the *stream function*, such that the velocity components in Z can be expressed as:

$$\begin{cases} u = \frac{\partial\psi}{\partial y} \\ v = -\frac{\partial\psi}{\partial x} \end{cases} \tag{20}$$

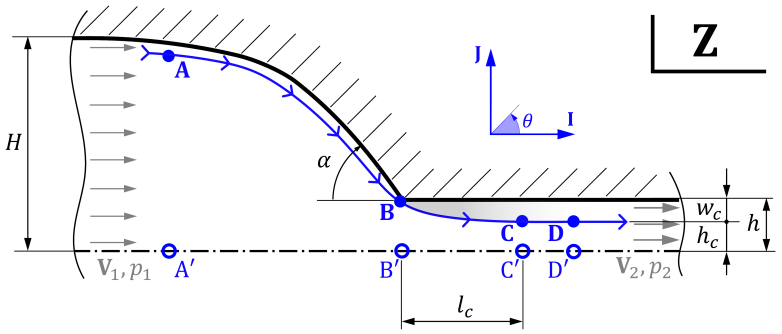

FIG. 2. Problem geometry and statement for the profiled nozzle. The free streamline is depicted as a solid blue line, showing the locations of the four points of interest **A**, **B**, **C** and **D**.

Hence, the complex conjugate of the velocity vector can be written as:

$$V_Z = \frac{dw}{dZ} \tag{21}$$

And the streamline profile in the Cartesian plane is straightforwardly obtained by integration:

$$Z = \int \frac{dw}{V_Z} \tag{22}$$

Unfortunately, the above expression cannot be evaluated until the complex velocity V_Z is not expressed as a function of w. In addition, the integral presented is, in fact, a *line integral* along the streamline profile in the complex w plane. Therefore, its transformation into a single-variate integral along the positive real axis is highly convenient. In order to map the complex potential plane to the positive real axis of an arbitrary t plane, the free streamline of interest must first be represented in the w plane. Although the velocity potential φ is part of the final solution, the magnitude of the stream function can readily be found out by integration:

$$\psi = \int u dy \tag{23}$$

For incompressible, inviscid flow in a two-dimensional geometry (featuring constant thickness b perpendicular to the Z plane), this stream function must be constant to ensure that continuity is fulfilled. Thus, it is only needed to evaluate ψ at the nozzle inlet, where:

$$\psi = \psi_A = \int_0^H |\mathbf{V}_1| dy = H|\mathbf{V}_1| \tag{24}$$

Applying continuity, the stream function will also be related to the outlet speed by:

$$\psi = \psi_D = \int_0^{h_c} |\mathbf{V}_2| dy = h_c|\mathbf{V}_2| = H\mu_c|\mathbf{V}_2| \tag{25}$$

In the light of the above, the complex potential representation of the sharp-edged and profiled nozzle hodographs is provided in figure 3.a. As the vertical coordiante of the projected axial points **A'**, **B'**, **C'** and **D'** is zero, their stream function is also null and they are located in the real axis. For the same reason, point **B.B'** is located at $\varphi = 0$, as it is forced to match the Cartesian origin of coordinates where $x = 0$. Points **A, A'** and **D, D'** are respectively located at upstream and downstream infinity,

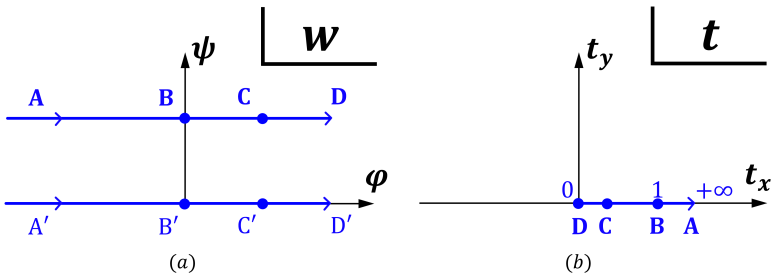

FIG. 3. Complex potential representation of the free streamline for the sharp-edged and profiled nozzle hodographs (a) and mapping to the ancillary domain t (b).

as it corresponds to their position in the Z domain. Finally, the velocity potential of **C, C'** is still unknown as the cavity endpoint cannot be known beforehand. Instead, the value of φ arising from the calculation will be used to determine the cavity length in Z.

Thus, the complex potential can be represented as shown in figure 3.a, taking the form of an *infinite strip* in the upper half (first and second quadrants) of the complex plane. Its mapping to the positive real axis is carried out through the well-known transform[42]:

$$w = i\,|\mathbf{V}_2|\,\mu_c H - \frac{|\mathbf{V}_2|\,\mu_c H}{\pi}\ln|t| \tag{26}$$

Applying this conformal map, the hodograph plane in 3.b is attained. Point **A** is mapped to $t=+\infty$, point **B** is mapped to $t=1$ and point **D** is mapped to $t=0$, while ensuring that point **C** will fulfill:

$$t_c \in (0,1) \tag{27}$$

If the integral of the free streamline profile is to be evaluated along t, a change of variable must be performed, for which the derivative of w with respect to t is retrieved:

$$\frac{dw}{dt} = -\frac{|\mathbf{V}_2|\,\mu_c H}{\pi}\frac{1}{t} \tag{28}$$

Finally, the streamline profile is expressed as:

$$Z = x + iy = -\int \frac{|\mathbf{V}_2|\,\mu_c H}{\pi}\frac{dt}{tV_Z} = C - \int_t^1 \frac{|\mathbf{V}_2|\,\mu_c H}{\pi}\frac{dt}{tV_Z} \tag{29}$$

where C is an integration constant. It should be remarked that the integral along t is evaluated between t and 1, as $t=1$ is the origin of the coordinate system. Integration from $t>1$ to $t=1$ can be used to compute the nozzle profile, while integration from $t<1$ to $t=1$ yields the cavity profile. At $t=1$, i.e. point **B**, it is known that the vertical coordinate of the streamline is equal to μH, so that the integration constant is:

$$i\mu H = C - \int_1^1 \frac{|\mathbf{V}_2|\,\mu_c H}{\pi}\frac{dt}{tV_Z} \implies C = i\mu H \tag{30}$$

The last step that is needed to undertake to find the streamline profile in the Cartesian plane is the conformal mapping of V_Z onto t, which follows a specific path for each nozzle geometry. For this reason, the hodograph transforms applied in the two cases under study will now be separated for the sake of clarity.

Point	Real part, $Re(\Omega)$	Imaginary part, $Im(\Omega)$
A	$ln(1/\mu_c)$	0
B	$ln(1/k)$	-α
C	$ln(1/k)$	0
D	0	0

TABLE II. Conformal mapping of the free streamline points in the sharp-edged nozzle onto the Ω plane.

A. Sharp-edged nozzle

The first step in the conformal mapping procedure for the sharp-edged nozzle hodograph comprises the definition of an ancillary Ω plane:

$$\Omega = \ln\frac{|\mathbf{V}_2|}{V_Z} = \ln\frac{|\mathbf{V}_2|}{|V_Z|} + i\theta \tag{31}$$

Following this transform, the coordinates of the V_Z points presented in table I are mapped to their new values in table II. As it has been previously stated, $k > 1$ and therefore the real part of Ω for **B** and **C** will be lower than or equal to zero, $Re(\Omega) \leq 0$. On the other hand, as $\mu_c < 1$ the real part of **D** will be strictly greater than zero, $Re(\Omega) > 0$. Finally, when dealing with a contracting nozzle, the angle α will be strictly greater than zero, meaning that the imaginary part of Ω at **B** will be strictly lower than zero, $Im(\Omega) < 0$. In addition, it is known that the axial points **A'**, **B'**, **C'** and **D'** have a constant argument $\theta = 0$, so they must be located along the real axis between **D** and **A**. With this information, the corresponding hodograph can be represented in the Ω plane, as depicted in figure 4. The path from **B** to **C** is covered at constant velocity (that is, the cavity interface velocity) and therefore the real part of Ω remains unchanged while the imaginary part ranges from $-i\alpha$ to 0. From **C** to **D**, the velocity modulus changes while the argument is kept constant. For this reason, the path in Ω is represented along the real axis, the same as for **D'**-**A'**.

The path from **A** to **B** is not known and its hodograph should be assumed, depending on the nozzle geometry. In a sharp-edged nozzle, the streamline would first need to undergo a slight deceleration while the velocity direction vector is directed towards the nozzle throat, followed by a quick acceleration (at constant $Im(\Omega)$) during the approximation to the throat corner **B**. In order to find an analytical solution to the problem, the shape of this streamline will be modeled as a quarter of ellipse. This simplification is intended to represent the best mathematical approximation to **B** from **A** that ensures a nearly constant inlet angle for the flow entering the throat as it corresponds to a sharp-edged nozzle, although the nozzle wall profile far upstream point **B** is not being represented with full accuracy.

At this point, it shall be reminded that the objective of the solution procedure is to map the Ω domain to the t real axis. For the sake of readability, the mapping process that will be followed in the forthcoming is summarized in figure 5. The original hodograph in Ω is first scaled and displaced to the fourth quadrant, after which it is mapped to a quarter of the unit circle in Ω''. From this point on, the mathematical derivation coincides with that of the notched hodograph proposed by Roshko[44], comprising the mapping to the first quadrant in Ω''', the mapping to the real and imaginary axes in χ and the final transform onto the t plane. The Roshko hodograph, originally derived for external flows, is used in the present derivation because it provides a steady-state solution and ensures the existence of a solution through the use of conformal mapping, even though it implicitly neglects re-entrant jet dynamics. After this preliminary overview, a more detailed explanation is now provided for each of these conformal mappings.

The first transformation that needs to be performed is the scaling and displacement of the hodograph in Ω to obtain a quarter of ellipse centered at the origin whose major axis has unit length. This is achieved through the Ω-Ω' transform, formulated as:

$$\Omega' = \frac{a}{a_0}\left(\Omega - \ln\left(\frac{1}{k}\right)\right) \tag{32}$$

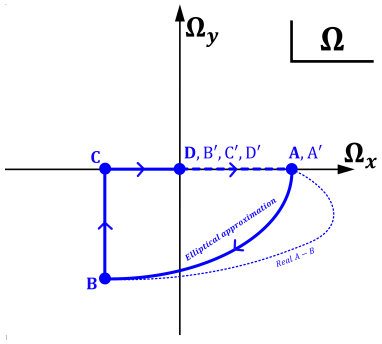

FIG. 4. Mapping to the Ω plane in the sharp-edged nozzle hodograph.

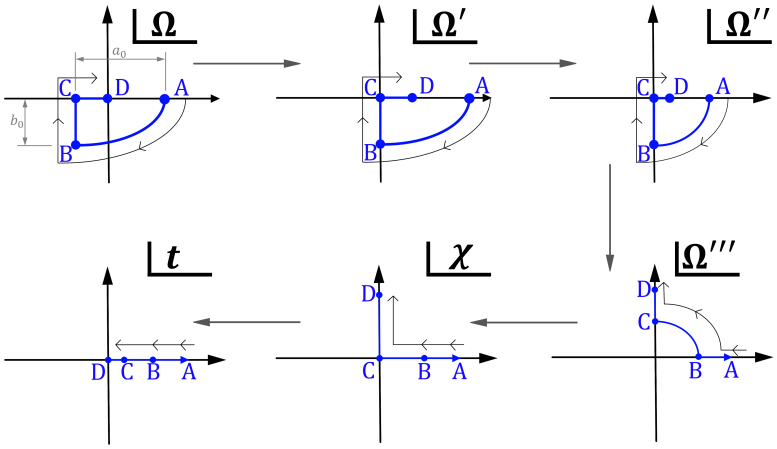

FIG. 5. Conformal mappings applied from the Ω to the t plane in the sharp-edged nozzle hodograph.

where a is a scaling parameter and a_0 the semi-major axis length in Ω. The scaling parameter a is given by:

$$a = \frac{1}{\sqrt{1-\left(\frac{b_0}{a_0}\right)^2}} \tag{33}$$

where b_0 stands for the semi-minor axis length in Ω.

The previous mapping was performed as a necessary requisite for the Schwarz transform to be applied[53]. This transform allows to map the interior and the perimeter of an ellipse with unitary semi-major axis to the interior and the perimeter of a unit circle, and has the form:

$$\Omega'' = \sqrt{\lambda}\ sn\left(\frac{2\kappa}{\pi}\ \arcsin\left(\Omega'\right), \lambda^2\right) \tag{34}$$

The evaluation of this transform is far more intricate than that of the previous ones, as it comprises

the use of the Jacobi elliptic function *sn* with parameter λ^2. The λ parameter is calculated by means of the Jacobi theta functions θ_2 and θ_3:

$$\lambda = \left(\frac{\theta_2(0,q)}{\theta_3(0,q)}\right)^2 \tag{35}$$

and the κ constant is also found using the theta function θ_3:

$$\kappa = \frac{\pi}{2}(\theta_3(0,q))^2 \tag{36}$$

where the Jacobi theta functions with nome q are calculated as follows[54]:

$$q = \left(a + a\frac{b_0}{a_0}\right)^{-4} \begin{cases} \theta_2(0,q) = 2q^{1/4}\sum\limits_{n=0}^{\infty}(-1)^n q^{n(n+1)} \\ \theta_3(0,q) = 1 + 2\sum\limits_{n=0}^{\infty} q^{n^2} \end{cases} \tag{37}$$

The application of this transform yields a quarter of the unit circle located in the fourth quadrant. Subsequently, the resulting hodograph is mapped onto the first quadrant in Ω''' so as to facilitate the subsequent steps:

$$\Omega''' = e^{-\frac{\pi}{2}i}\left(\frac{\Omega''+1}{\Omega''-1}\right) \tag{38}$$

The circle perimeter is now projected on the positive real and imaginary axes, for which the Joukowsky[45] transform is retrieved:

$$\chi = \frac{1}{2}\left(\Omega''' + \frac{1}{\Omega'''}\right) \tag{39}$$

Finally, the Roshko[44] transform is applied to map the hodograph in χ to the t axis:

$$t = \frac{\Lambda^2 + \chi^2}{\Lambda^2 + 1} \tag{40}$$

where the ancillary constant Λ is given by:

$$\Lambda = \frac{\gamma^2 - 1}{2\,\gamma}\ ,\ \gamma = \frac{1+\chi_D}{1-\chi_D} \tag{41}$$

with χ_D denoting the complex coordinates of point D in the χ plane (purely imaginary).

At this point, the relationship between Ω and t has been fully derived. However, the use of the Schwarz transform in 34 greatly increases the difficulty of an analytical evaluation of the integral, which should instead be calculated numerically in the *Results and discussion* section.

B. Profiled nozzle

The initial transformation to be performed in the profiled nozzle case is identical to that used for the sharp-edged nozzle. Despite this, the new hodograph plane will be named Γ so as to allow an easier differentiation:

$$\Gamma = \ln\frac{|\mathbf{V}_2|}{V_Z} = \ln\frac{|\mathbf{V}_2|}{|V_Z|} + i\theta \tag{42}$$

Downstream point **B**, the hodographs for the sharp-edged and profiled nozzles are coincident, and the difference between both cases lies upon the shape of the approximation path **A**-**B**. Clearly, the shortest approach in Γ is a straight line, as employed by Howe[42] for the discharge of a jet from a

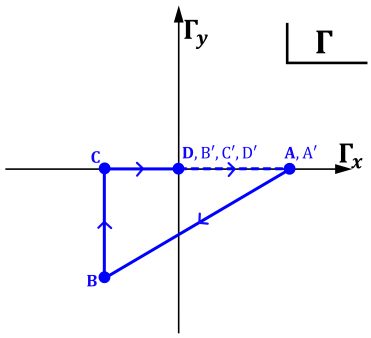

FIG. 6. Mapping to the Γ plane in the profiled nozzle hodograph.

profiled nozzle. Under this simplification, the hodograph in Γ has the appearance shown in figure 6. The fact that the shape of the hodograph is a triangle allows to apply the Schwarz-Christoffel transform, that maps the interior of any polygon to the complex upper-half plane. Consequently, the perimeter of the polygon is mapped to the real axis, which can conveniently be chosen to match the t plane. The Schwarz-Christoffel map $f(t)$ from the upper half of the complex plane to the interior of any polygon is given by Driscoll[53]:

$$f(t) = f(t_0) + C\int_{t_0}^{t}\prod_{j=1}^{n-1}(\zeta - t_j)^{\alpha_j - 1}d\zeta \tag{43}$$

where t_j represent the *prevertices* of the polygon in the t plane, such that:

$$t_1 < t_2 < \ldots < t_n = \infty \tag{44}$$

and $\pi\alpha_j$ are the interior angles at the j^{th} vertices, fulfilling that:

$$\sum_{j=1}^{n}\alpha_j = n - 2 \tag{45}$$

From this definition, it becomes clear that:

- One of the prevertices (in this case, the one corresponding to point **A**) must be located at infinity in the t plane.
- The transformation has three degrees of freedom (Möbius transformation), and therefore three of the prevertices can be chosen beforehand. As the t_n prevertex is already fixed, two degrees of freedom are left for the remaining prevertices.
- If more than two prevertices are left, their values cannot be arbitrarily assumed, and the numerical solution of a so-called Scwharz-Christoffel problem is required[53].

Trivially, when dealing with a triangular hodograph only three prevertices are commonly needed. However, in the present problem a fourth vertex **D** is introduced. The location of this vertex in t must coincide with the origin of the complex plane, and this cannot be guaranteed if the mapping $f(t)$ is found using **A**, **B** and **C** as prevertices. In addition, the prevertex t_C corresponding to point **C** is not known, meaning that it cannot be used to compute the parameters of the transformation.

A convenient choice of the t_0 prevertex, forcing it to match the coordinate $t_D = 0$ for point **D**, allows to solve the Schwarz-Christoffel problem enunciated above:

$$f(t) = C\int_{0}^{t}\prod_{j=1}^{n-1}(\tau - t_j)^{\alpha_j - 1}d\tau \tag{46}$$

In addition, t_A , t_B and t_C are chosen as the prevertices, whose corresponding vertices in Γ are respectively located at:

$$\begin{cases} \Gamma_A = ln(1/\mu_c), t_A = \infty \\ \Gamma_B = ln(1/k) - i\alpha, t_B = 1 \\ \Gamma_C = ln(1/k), t_C = c \end{cases} \tag{47}$$

It should be highlighted that an additional unknown c has arisen, standing for the coordinate of point **C** in the real axis t of the transformed plane. Hence, two unknowns, namely C and c, must be found in order to fully define $f(t)$. Using the available information, a nonlinear system of two equations can be formulated:

$$\begin{cases} \Gamma_B = f(1) = ln(1/k) - i\alpha = C\int_0^1 \frac{d\tau}{(\tau-c)^{\frac{1}{2}}(\tau-1)^{\frac{\nu}{\pi}+\frac{1}{2}}} \\ \Gamma_C = f(c) = ln(1/k) = C\int_0^c \frac{d\tau}{(\tau-c)^{\frac{1}{2}}(\tau-1)^{\frac{\nu}{\pi}+\frac{1}{2}}} \end{cases} \tag{48}$$

where ν is the internal angle at B in the Γ plane, namely:

$$\nu = \arctan\left(\frac{\alpha}{ln(1/\mu_c) - ln(1/k)}\right) \tag{49}$$

From $\Gamma_B = f(1)$, the value of the constant C can be extracted:

$$C = \frac{ln(1/k) - i\alpha}{\int_0^1 (\tau-c)^{-\frac{1}{2}}(\tau-1)^{-\frac{\nu}{\pi}-\frac{1}{2}}d\tau} \tag{50}$$

And, by plugging this constant in the $\Gamma_C = f(c)$ equality, the final nonlinear equation to be solved is found:

$$\underbrace{\frac{ln(1/k) - i\alpha}{\int_0^1 (\tau-c)^{-\frac{1}{2}}(\tau-1)^{-\frac{\nu}{\pi}-\frac{1}{2}}d\tau}\int_0^c \frac{d\tau}{(\tau-c)^{\frac{1}{2}}(\tau-1)^{\frac{\nu}{\pi}+\frac{1}{2}}}}_{LHS} = \underbrace{ln(1/k)}_{RHS} \tag{51}$$

For this equality to be met, the imaginary part of the left hand side LHS must be zero as the right hand side RHS is a pure real number. What is more, this real part must be equal to $ln(1/k)$. As a result of the previous steps, the only possible value of c that makes $Im(LHS) = 0$ is the one that yields $LHS = RHS$ because c has already been implicitly introduced in the equation through the angle ν. In figure 7, this is shown for a case in which:

$$\begin{cases} \alpha = \pi/2 \\ \mu_c = 0.1 \\ k = 1.5 \end{cases} \tag{52}$$

By plotting $Im(LHS)$ in solid lines and $Re(LHS)$ in dashed lines, it can be checked that the only value of c for which it holds that $LHS = RHS$ is also the only value of c for which $Im(LHS) = 0$. This graphical representation can therefore be used to show intuitively that the conformal map $f(t)$ that is calculated by solving for c is a unique solution for the Schwarz-Christoffel problem.

Using the value of c that has been derived from the previous computation as defined in figure 7, the dummy plane t can be related to the hodograph plane Γ through $f(t)$. It shall be remarked that, although the mathematical complexity of the transformation is greater than that of the sharp-edged nozzle, the mapping from Γ to t has been performed in a single step for this case.

C. Integration

Through conformal mapping, the relationship between the hodographs Ω, Γ and the real axis t has been derived for both the cavitating sharp-edged and profiled nozzles. The final step of the

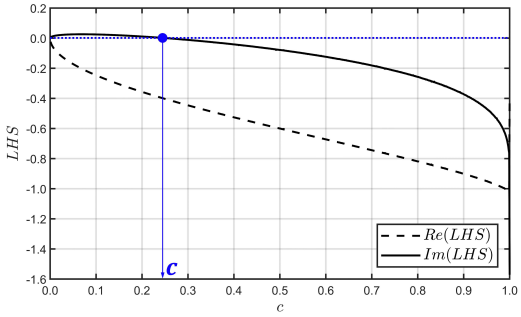

FIG. 7. Graphical representation of the numerical solution for the Schwarz-Christoffel mapping in the profiled nozzle hodograph, showing the uniqueness of the solution.

solution procedure is the introduction of these expressions in equation (29), substituting V_Z:

$$\begin{cases} Z(t) = i\mu H - \frac{\mu_c H}{\pi} \int_t^1 \frac{e^{\Omega(\tau)}}{\tau} d\tau \ \ (sharp-edged) \\ Z(t) = i\mu H - \frac{\mu_c H}{\pi} \int_t^1 \frac{e^{\Gamma(\tau)}}{\tau} d\tau \ \ (profiled) \end{cases} \tag{53}$$

As it has been previously stated, values of $t > 1$ yield the points of the nozzle wall while $t < 1$ represents the free streamline profile. Hence, the zone of interest for practical purposes is the interval $t \in (0,1)$: the cavity profile is described between t_B and t_C, while the cavity wake where vapor condensation takes place is located between t_C and t_D.

In order to directly obtain the section reduction μ_c without evaluating the whole interval t_B-t_C, an asymptotic solution similar to the one proposed by Howe [42] can be used. At downstream infinity, namely at $t \to 0$, the imaginary part of the streamline complex coordinate $Im(Z)$ will be equal to $\mu_c H$. Therefore, $Z(0)$ in equation (53) can be replaced by $i\mu_c H$ and the resulting expression can be solved for the geometrical nozzle contraction μ:

$$\begin{cases} \mu = \mu_c \left(1 + \frac{1}{\pi} Im\left(\int_t^1 \frac{e^{\Omega(\tau)}}{\tau} d\tau\right)\right) (sharp-edged) \\ \mu = \mu_c \left(1 + \frac{1}{\pi} Im\left(\int_t^1 \frac{e^{\Gamma(\tau)}}{\tau} d\tau\right)\right) (profiled) \end{cases} \tag{54}$$

The results arising from the application of the presented model will be commented in the following section, in which a comparison with experiments and numerical multiphase calculations is also included.

IV. RESULTS AND DISCUSSION

The derived model has the capability to predict cavity width, length and shape for different nozzle geometries as a function of the cavitation number σ and the nozzle contraction ratio μ. For this reason, it has been considered appropriate to present the results in the form of graphs relating these variables along a range of geometrical parameters. The aim of this format is to provide a direct graphical tool for engineers working in the early stages of injector development, where a quick check on cavitation occurrence and expected cavity size can significantly streamline the design process. The following variables will be presented for nozzle contraction ratios between $\mu = 0.05$ and $\mu = 0.25$ in 3 intervals, each of which will cover nozzle angles α between 90° and 30°, in 15° intervals:

- The non-dimensional cavity width, w_c/h , as deduced from equation (54).

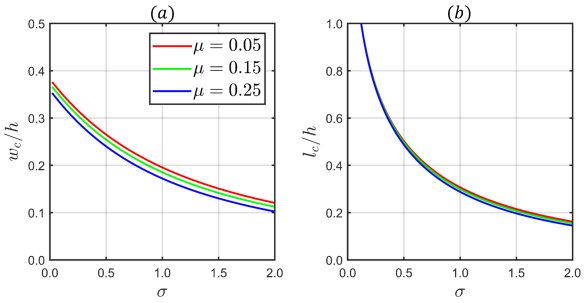

FIG. 8. Dependence on σ of the non-dimensional cavity width (a) and length (b) for a sharp injector with $\alpha = 90°$.

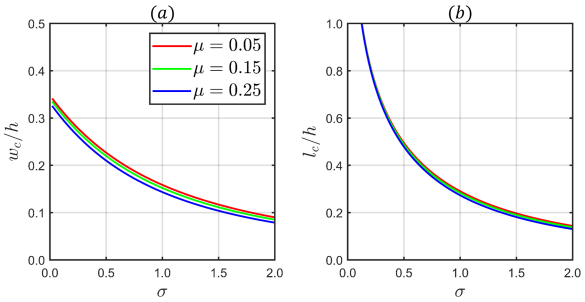

FIG. 9. Dependence on σ of the non-dimensional cavity width (a) and length (b) for a sharp injector with $\alpha = 75°$.

- The non-dimensional cavity length, l_c/h (between **B** and **C**), obtained as the real part of the solution for equation (53) when $t = c$.

This information will be displayed for both the sharp-edged and the profiled nozzle geometries, and an additional *Validation* section is provided so as to compare the performance of the proposed model with experimental data.

A. Sharp-edged nozzle

The analytical results of predicted cavity width and length for the sharp-edged nozzle are provided in figure 8, figure 9, figure 10, figure 11 and figure 12, each corresponding to $\alpha = 90°$, $\alpha = 75°$, $\alpha = 60°$, $\alpha = 45°$ and $\alpha = 30°$, respectively. In all cases, the cavity width increases with decreasing cavitation number up to a bounded magnitude at $\sigma = 0$. Conversely, the cavity length exhibits an asymptotic growth at $\sigma \to 0$, where l_c/h tends to infinity. A comparison between the results at different contraction coefficients for any nozzle wall angle α immediately reveals that stronger contractions (lower μ) lead to increased cavitation proneness. The evolution of the cavity size with the contraction ratio is not linear. Instead, cavity growth is accentuated near the smallest values of μ. This trend must not be attributed to a higher flow speed when decreasing the throat section, as the cavitation number σ has been defined with respect to the outlet velocity. Instead, the flow

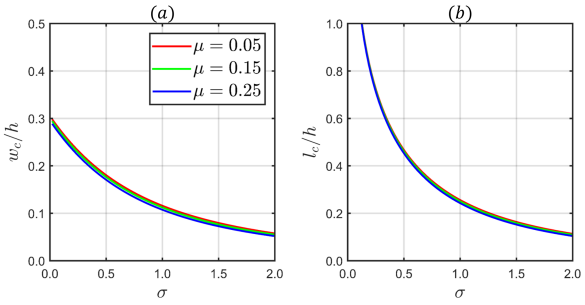

FIG. 10. Dependence on σ of the non-dimensional cavity width (a) and length (b) for a sharp injector with $\alpha = 60°$.

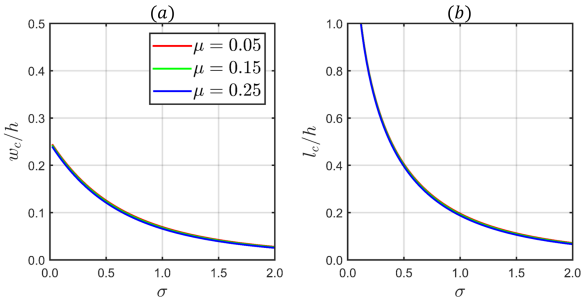

FIG. 11. Dependence on σ of the non-dimensional cavity width (a) and length (b) for a sharp injector with $\alpha = 45°$.

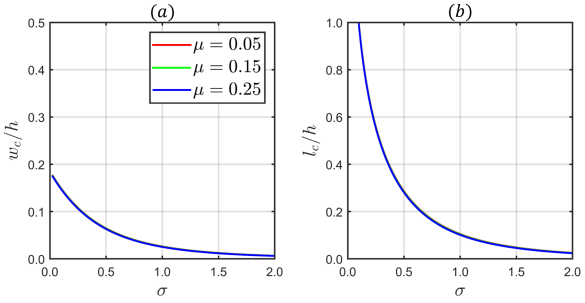

FIG. 12. Dependence on σ of the non-dimensional cavity width (a) and length (b) for a sharp injector with $\alpha = 30°$.

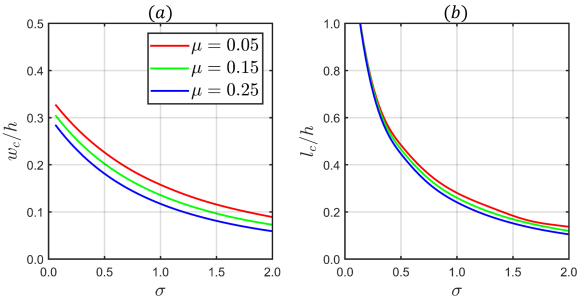

FIG. 13. Dependence on σ of the non-dimensional cavity width (a) and length (b) for a profiled injector with $\alpha = 90°$.

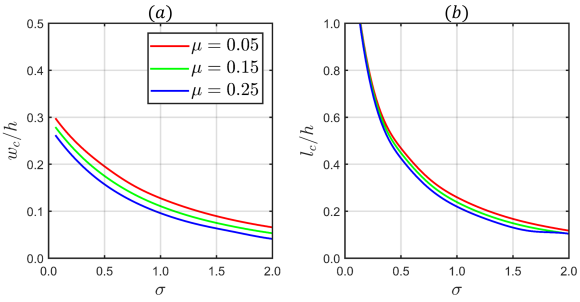

FIG. 14. Dependence on σ of the non-dimensional cavity width (a) and length (b) for a profiled injector with $\alpha = 75°$.

mechanism explaining this increase in relative cavity size is the sharpness of the approach towards point **B**, which enhances separation at low μ and thus increases the *vena contracta* effect. This reasoning is reinforced by the reduction of differences in cavity width and length as the α angle is lowered. Under the conditions being studied, flow separation and the *vena contracta* are the mechanisms leading to the formation of vapor cavities.

Attending to the presented results, the nozzle angle is also shown to play a key role on cavity development. The reasons for this effect coincide with those motivating the appearance of larger cavities at lower contraction ratios: when the approach angle α is sharper (i.e., closer to 90°), the flow is separated and cavities form in the low pressure region. In real practice, milder approach angles lead to longer and more slender nozzles (especially at low contraction ratios) which may not be desirable from a manufacturing point of view. In any case, the influence of the α angle is clearly greater than that of the contraction ratio μ.

B. Profiled nozzle

The analytical results of predicted cavity width and length for the profiled nozzle are provided in figure 13, figure 14, figure 15, figure 16 and figure 17, each corresponding to $\alpha = 90°$, $\alpha = 75°$, $\alpha = 60°$, $\alpha = 45°$ and $\alpha = 30°$, respectively. The trends observed for the profiled nozzle are analogous to those obtained in the sharp-edged case, with the cavity size increasing at smaller

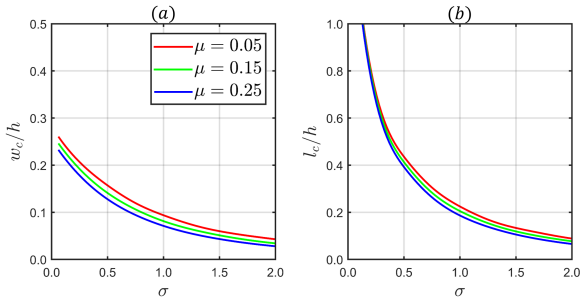

FIG. 15. Dependence on σ of the non-dimensional cavity width (a) and length (b) for a profiled injector with $\alpha = 60°$.

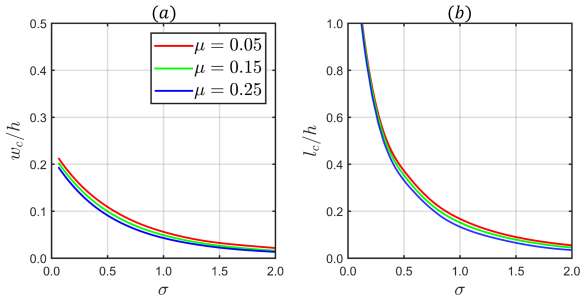

FIG. 16. Dependence on σ of the non-dimensional cavity width (a) and length (b) for a profiled injector with $\alpha = 45°$.

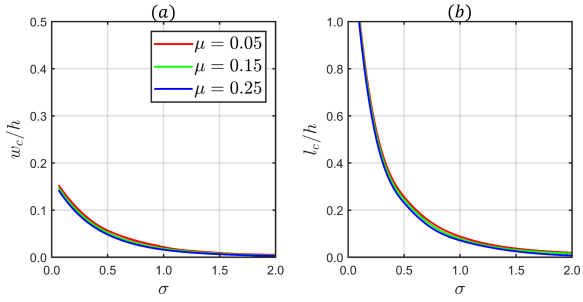

FIG. 17. Dependence on σ of the non-dimensional cavity width (a) and length (b) for a profiled injector with $\alpha = 30°$.

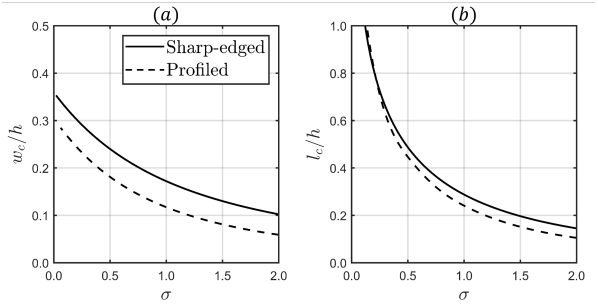

FIG. 18. Comparison of cavity features, namely width (a) and length(b), for the sharp-edged and the profiled nozzle geometries at $\alpha = 90°$ when $\mu = 0.25$.

Parameter	Value
Liquid density, ρ_L	850 kg/m^3
Vapour pressure, p_V	0.02 bar
Inlet pressure, p_1	100 bar
Contraction ratio, μ	0.05
Nozzle wall angle, α	90°

TABLE III. Fluid properties and geometrical parameters in the Winklhofer *et al.* [46] cavitating nozzle experiments.

contraction ratios μ and sharper wall angles α . The differences observed at different values of μ, however, become more evident in the profiled nozzle at every value of α. This difference with the sharp-edged case takes place because the dominating flow separation mechanism is not the nozzle sharpness in terms of wall curvature but its abruptness regarding the contraction ratio. In the sharp-edged geometry, these differences at variable μ are overshadowed by the sudden curvature change near point **B**.

A comparison between figures 8 and 13, however, shows that the influence of the nozzle geometry is greater than the effect of the nozzle contraction ratio. In order to facilitate this comparison, figure 18 shows the cavity width and length for both the sharp-edged and the profiled nozzles at $\mu = 0.25$ and $\alpha = 90°$. The greatest differences arise for the cavity width w_c, which is consistently greater in the sharp-edged case through the whole range of σ. Regarding the cavity length l_c, it is also greater for the sharp-edged nozzle, although both geometries approach asymptotically as $\sigma \to 0$.

C. Validation

Although the prediction of cavity shape characteristics is interesting from a design perspective, the most important effect of in-nozzle cavitation is flow choking. Using the results provided above, the choking characteristics of a cavitating nozzle can be predicted, their value being used as a tool for the validation of the model with respect to experimental results. In this spirit, the experimental work of Winklhofer *et al.* [46] is chosen as a benchmark because it is based on a true-scale ($284\mu m$ nozzle width), two-dimensional sharp-edged injector. The fluid properties and geometrical parameters that describe this experiment are summarized in table III.

In order to validate the analytical model being presented, the choking characteristics from the Winklhofer *et al.* [46] experiment are being compared with the outcomes of the free streamline method. For this purpose, the relationship between the cavitation number σ and the cavity width w_c

is retrieved and introduced into a simplified head loss model that will allow to quantify the Δp-$\dot{m}$ curve that characterizes the cavitating behavior of an injector.

The detailed derivation of the mass flow choking model can be found in Appendix A, in which control volume theory and ideal flow assumptions are applied to obtain the mass flow rate as a function of the cavitation constant k:

$$\dot{m} = \rho_L \, h \, b \, \frac{\mu_c}{\mu} \sqrt{\frac{2(p_1 - p_V)}{\rho_L \left[\mu_c^2 \left(\frac{1}{\mu_c} - 1 \right)^2 + k^2 - 1 \right]}} \tag{55}$$

Where b is the nozzle width, measured along a direction perpendicular to the Z plane. The pressure drop is computed following the classical equation arising from control volume theory[48], namely:

$$\Delta p = \frac{1}{2} \rho_L |\mathbf{V}_2|^2 \; \mu_c^2 \left(\frac{1}{\mu_c} - 1 \right)^2 \tag{56}$$

where $|\mathbf{V}_2|$ is calculated from the mass flow rate (equation (55)). The results from Winklhofer *et al.*[46] are not expressed as a function of the cavitation number σ, but as a function of the modified cavitation number CN instead:

$$CN = \frac{p_1 - p_2}{p_2 - p_V} \tag{57}$$

This modified cavitation number can easily be expressed as a function of the cavitation constant k, as:

$$CN = \frac{{\mu_c}^2 \left(\frac{1}{\mu_c} - 1 \right)^2}{k^2 - 1} \tag{58}$$

This way, the mass flow rate $\dot{m}$, the pressure jump Δp and the modified cavitation number CN have been expressed as a function of the solution parameters of the analytical model, namely k and μ_c. Applying the above equations (55), (56) and (58), a comparison between the results arising from the application of the present model and those obtained by Winklhofer *et al.*[46] is provided in figure 19. In this figure, the numerical results obtained by Payri *et al.*[47] from numerical multiphase simulations applying the Schnerr-Sauer[35] model are also represented. The evolution of the non-dimensional mass flow rate (calculated as the ratio between the mass flow rate $\dot{m}$ and the choked mass flow rate $\dot{m}_\infty$) is tracked at a variable (modified) cavitation number CN. Using this definition of the modified cavitation number, commonly used in the field of injection systems, a higher CN will lead to more severe cavitation conditions (i.e., cavitation intensity increases from left to right in the horizontal axis), as opposed to using the σ alternative.

The mass flow rate follows a rapid (nearly exponential) growth at low magnitudes of CN, but reaches an asymptotic value $\dot{m}/\dot{m}_\infty \to 1$ at increasing cavitation number due to the section contraction encompassed by a further increase of Δp in cavitating conditions. To characterize this phenomenon, a critical cavitation number CN_c is defined as the value of CN that yields $\dot{m}/\dot{m}_\infty = 0.99$. The critical cavitation numbers obtained using the analytical model and the numerical CFD calculation are summarized in table IV. From these results, it is found that the performance of the analytical model regarding the choked cavitation number prediction, with a 24% relative error, is even better than that of the CFD calculation (for which a 60% error is obtained). What is more, the global shape of the $CN - \dot{m}$ characteristics is faithfully replicated for the whole range of CN under study, the greatest discrepancy arising in noncavitating conditions (i.e., at low CN). This is explained by the fact that, under such conditions, the flow in the throat section remains attached and the head loss mechanism is governed by wall friction and viscous effects (also owing to turbulence), which are not considered by potential flow. For this reason, the mass flow rate is overestimated by the free streamline solution in a noncavitating regime. Nevertheless, as soon as the critical cavitation number is approached and flow detachment begins, the accuracy of the analytical solution increases. Overall, the analytically determined mass flow choking curve closely matches the experimental measurements.

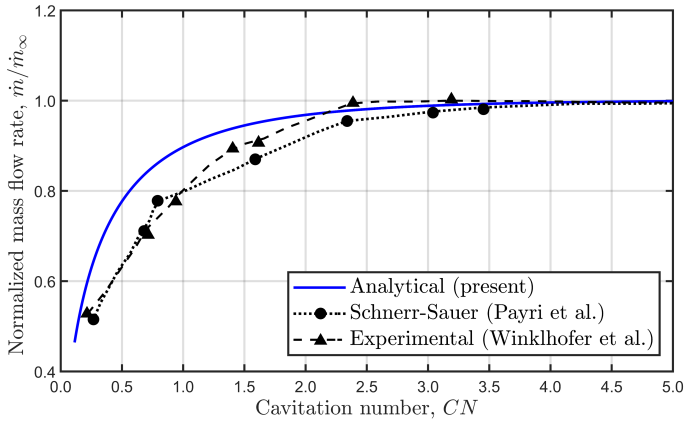

FIG. 19. Mass flow choking characteristics of the two-dimensional injector with $\mu = 0.05$ and $\alpha = 90°$ obtained from the analytical model (blue, solid line), the experiments from Winklhofer *et al.* [46] (black triangles, dashed line) and the numerical simulation from Payri *et al.* [47] (black circles, dotted line).

Parameter	CN_c	Relative error (%)
Experimental	2.5	0%
Numerical	4.0	60%
Analytical	3.1	24%

TABLE IV. Comparison of the critical cavitation number CN_c obtained from the analytical model with the numerical calculation by Payri *et al.* [47] and the experiments by Winklhofer *et al.* [46].

Besides the previously commented mass flow choking curves, Winklhofer *et al.* [46] also provide void fraction contours observed at different cavitation regimes. These contours are based on light transmittance maps acquired by means of back illumination using a CCD camera, and can be compared to the cavity profiles given by equation (29). In order to extend the capabilities of the analytical model, a Homogeneous Relaxation Model (HRM) has been coupled to the free streamline solution as described in Appendix B. This model, based on the application of empirically calibrated coefficients for evaporation and condensation, is only applied to model cavity condensation, as it will be assumed that the vapor volume fraction β is equal to 1 in the cavity region. The use of HRM in this model is limited to the cavity morphology calculation, as the cavity length and width, as well as the mass flow choking characteristics, were calculated using purely analytical methods.

The static pressure p profile along the cavity condensation part of the free streamline is derived assuming ideal flow:

$$p = p_2 - \frac{1}{2}\rho_L \left(|\mathbf{V}|^2 - |\mathbf{V}_2|^2\right) \tag{59}$$

where the velocity modulus $|\mathbf{V}|$ is an outcome of the potential flow solution, being a function of the axial (horizontal) coordinate x. In figure 20, the experimental void fraction contours (a) are compared to their analytical counterparts (b) obtained from potential flow-HRM coupling, as well as the numerical results by Payri *et al.* [47], both using an HRM model (c) and the Schnerr-Sauer model (d). Instead of using the cavitation number σ or CN to characterize the flow, the pressure jump Δp is preferred in this case because it provides a more practical approach related to the working conditions of the nozzle.

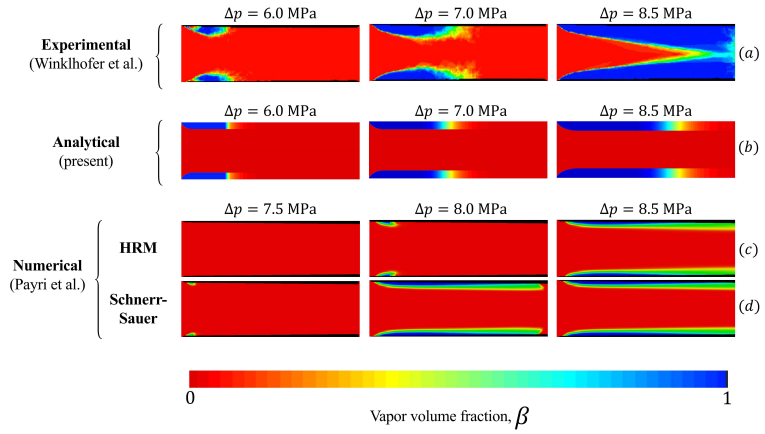

FIG. 20. Comparison of experimental cavity morphology([46] (a) with the potential flow-HRM coupled solution (b) and the numerical results obtained by Payri *et al.* [47] applying the HRM (c) and the Schnerr-Sauer (d) models. Reproduced with permission from the Journal of the Brazilian Society of Mechanical Sciences and Engineering 43,228 (2021). Copyright 2021 Springer Nature.

The experimental data in (a) show that cavity growth occurs both in the longitudinal (length l_c) and vertical (width w_c) directions when the pressure jump is increased while keeping a constant injection pressure. Choked conditions correspond to $\Delta p = 8.5$ MPa, at which the cavities developed on both sides of the nozzle throat coalesce to form a pure vapor flow. For the three magnitudes of Δp analyzed, cavity growth begins in the inlet corner of the throat section, confirming the assumption that was applied during the derivation of the theoretical model. Regarding the results obtained from the application of the presented analytical model (b), the cavity length and width observed in the experiments are faithfully replicated at $\Delta p = 6.0$ MPa and $\Delta p = 7.0$ MPa. At $\Delta p = 8.5$ MPa, however, the cavity width is underestimated by the analytical solution and the coalescence of cavities is not predicted. The reasons for this discrepancy lie on the facts that the cavity endpoint has been assumed to have $\theta = 0°$ (which is not fulfilled in this case), the assumption of pure liquid flow at the nozzle outlet (in this case, it is fully vaporized) and the neglection of turbulent mixing, which plays a crucial role in this type of cavity growth. Nevertheless, the cavity morphology in the near-inlet zone is reproduced with a very high accuracy. In any case, the analytical results represent a significant improvement with respect to the numerical multiphase model in (c) and (d). It should be remarked that neither the HRM (c) nor the Schnerr-Sauer (d) model are able to predict cavitation inception at $\Delta p < 7.5$ MPa, while the analytical solution allows to model cavities even at $\Delta p = 6.0$ MPa. In addition, the cavity width predicted by the analytical model is closer to the experimental results than that computed by CFD using Schnerr-Sauer and HRM. The validation methodology has shown that the proposed analytical formulation is able to closely replicate the steady characteristics of in-nozzle cavitation. What is more, the accuracy of the analytical results even outperforms CFD calculations at the near-choked condition. The cavity morphology, mass flow and pressure jump at variable working parameters can be predicted by the model for a given injector geometry and working fluid.

V. CONCLUSIONS

An analytical free-streamline solution for the cavitating flow inside a nozzle is derived applying potential flow theory and conformal mapping. Two solution methods are presented, corresponding to sharp-edged and profiled nozzle shapes. In both cases, the non-dimensional cavity width and

length are calculated as a function of the cavitation number σ and the nozzle contraction ratio μ. The formulation also allows to vary the nozzle wall angle α, with results for $\alpha = 30°$, 45°, 60°, 75° and 90° being provided in the present article. In addition, the differences in the cavity morphologies observed in the sharp-edged and profiled nozzles are studied, quantifying the influence of geometrical parameters.

The mathematical model being presented is based on necessary assumptions and simplifications, namely: inviscid, incompressible and irrotational flow and homogeneous phase equilibrium (i.e., instantaneous evaporation below p_V). These simplifications are needed to guarantee the existence of a unique solution to the free streamline problem. Comparison with experimental results[46] shows that the assumptions being applied are not detrimental to the model accuracy. The mass flow and pressure jump characteristics, as well as the void fraction contours, are faithfully replicated by the analytical solution. When working close to the critical cavitation number (i.e., near-choked flow), the analytical model even outperforms CFD calculations.

The prediction and control of geometrical cavitation plays a critical role in the design of modern injection and atomization systems. Cavitation in water, diesel fuel or ammonia is a source of trouble during the development stage of such fluid systems. The presented analytical solution is intended not only to fill a theoretical knowledge gap in the field but also to provide a quick design tool for engineers. The information included in figures 8-17 can be used during preliminary design processes to obtain a quick check on cavitation occurrence, or incorporated into more complex design optimization algorithms without requiring the use of time-consuming CFD simulations. Information about cavity shape and size, as well as its influence on mass flow, can be extracted from the proposed equations.

The theoretical model hereby presented paves the way for future developments aimed at enriching the theoretical background on cavitation. Model improvements such as the introduction of unsteady potential flow effects, the derivation of a model for asymmetric nozzles, or the quantification of the injector needle lift influence are to be considered. In addition, the accuracy of the model could benefit from the application of a re-entrant jet boundary condition, in accordance with experimental evidence.

ACKNOWLEDGEMENTS

Authors acknowledge that this work was partially funded by Universidad de Oviedo and LINTER TECHNICAL CENTER, S.L., under the project "FUO-25-024: Modelo numérico 3D de la atomización de fluidos viscosos para la aplicación de tratamientos superficiales". Álvaro Pardo Vigil is supported by the Spanish Ministry of Science, Innovation and Universities within the "FPU" Program (grant reference FPU23/03450). Additional funding is provided by Agencia de Ciencia, Competitividad Empresarial e Innovación Asturiana (Sekuens) within "Subvenciones a Grupos de Investigacion de Organismos Publicos de I+D+I del Principado de Asturias, Convocatoria 2024" (grant reference IDE/2024/000724).

AUTHOR DECLARATIONS

The authors report no conflict of interest. **CRediT author statement**: **Alvaro Pardo-Vigil**: conceptualization, methodology, writing-original draft preparation, visualization, investigation. **José González Pérez**: methodology, visualization, writing-original draft, supervision. **Adrián Pandal**: conceptualization, methodology, formal analysis, writing-review and editing, supervision.

DATA AVAILABILITY STATEMENT

The data that support the findings of this study are openly available in Repositorio Institucional de la Universidad de Oviedo at `http://doi.org/10.17811/ruo_datasets.79308`, reference number 79308.

Appendix A: Mass flow choking equations

A simplified analytical model is used to calculate the relationship between the pressure jump across the injector nozzle Δp and the mass flow rate $\dot{m}$. As the liquid phase is considered to be incompressible, the mass flow rate is given by:

$$\dot{m} = \rho_L b h_c |\mathbf{V}_2| \tag{A1}$$

where b is the nozzle width, measured along a direction perpendicular to the Z plane. The contracted flow height h_c is found from the cavity contraction ratio μ_c:

$$h_c = h\frac{\mu_c}{\mu} \tag{A2}$$

As h_c is known to be a function of the cavitation number (or, equivalently, to the cavitation constant k), finding the dependence of $|\mathbf{V}_2|$ on k will allow to express the mass flow as a function of the cavitation number.

If the relationship between $\dot{m}$ and Δp is also to be found, then the head losses as a function of k must be determined. Following Ambrose [48], the equation for the head losses in a sudden contraction (deduced from control volume theory[55]) can be applied:

$$\Delta p = \rho_L \frac{|\mathbf{V}_1|^2}{2}\left(\frac{1}{\mu_c}-1\right)^2 = \rho_L \frac{|\mathbf{V}_2|^2}{2}\mu_c^2\left(\frac{1}{\mu_c}-1\right)^2 \tag{A3}$$

In equations (A1) and (A3), the mass flow rate and the pressure jump have been expressed as a function of the cavity contraction μ_c and the outlet velocity modulus $|\mathbf{V}_2|$. Although μ_c is known to be a function of the cavitation number, their relationship being extensively described in the *Results* section, the value of $|\mathbf{V}_2|$ remains unsolved. Hence, the definition of the cavitation number σ must be used in order to obtain a different expression for the pressure jump:

$$\begin{gathered}\sigma = k^2 - 1 = \frac{p_1 - \Delta p - p_V}{\frac{1}{2}\rho_L |\mathbf{V}_2|^2} \rightarrow \\ \rightarrow \Delta p = p_1 - p_V - \frac{1}{2}\rho_L |\mathbf{V}_2|^2 (k^2-1)\end{gathered} \tag{A4}$$

If both equations (A3) and (A4) for Δp are combined, the outlet velocity is obtained as a function of the inlet pressure p_1 and the cavitation constant k:

$$|\mathbf{V}_2| = \sqrt{\frac{2(p_1 - p_V)}{\rho_L\left[\mu_c^2\left(\frac{1}{\mu_c}-1\right)^2 + k^2 - 1\right]}} \tag{A5}$$

The contraction ratio μ_c also appears in the expression, but it must be reminded that it has a known dependence on k (or σ). Hence, equation (57) can be plugged into (A1) to find the mass flow rate, while the substitution of $|\mathbf{V}_2|$ in equation (A4) allows to calculate the pressure drop for a given cavitation number σ or cavitation constant k.

Finally, the modified cavitation number CN can also be found from k, following:

$$\begin{gathered}CN = \frac{p_1 - p_2}{p_2 - p_V} = \frac{\Delta p}{\frac{1}{2}\rho_L |\mathbf{V}_2|^2\, \sigma} = \\ = \frac{\Delta p}{\frac{1}{2}\rho_L\, |\mathbf{V}_2|^2\, (k^2-1)} = \frac{{\mu_c}^2\left(\frac{1}{\mu_c}-1\right)^2}{k^2-1}\end{gathered} \tag{A6}$$

In this way, the mass flow rate $\dot{m}$, pressure jump Δp and modified cavitation number CN have been expressed as a function of k, and the presented equations are used to validate the proposed model with respect to the experimental results of Winklhofer *et al.* [46].

Appendix B: Homogeneous Relaxation Model for cavity morphology

The Homogeneous Relaxation Model (HRM), as proposed by Bilicki and Kestin [56] for multiphase flows based on the proposal by Einstein [57] in gas flow, is applied to model cavity condensation, thus allowing to represent an estimated cavity morphology (HRM is not used to calculate the cavity length, width or mass flow choking, as these are obtained from the purely analytical method being presented in this article). The model constants calculated for flash boiling by Downar-Zapolski *et al.* [58] are applied, introducing an empirically determined correction factor to account for the differences between water and diesel fuel.

The HRM model describes the Lagrangian phase change rate for the vapor mass fraction Y_v with respect to its equilibrium value at the working pressure and temperature as:

$$S_V = \frac{DY_V}{D\mathscr{T}} = \frac{\overline{Y}_{V,eq} - Y_v}{\Theta} \tag{B1}$$

where Θ is a characteristic timescale that must be found empirically through correlations, and $\mathscr{T}$ is the dimensional time. Downar-Zapolski *et al.* [58] propose two different equations for Θ:

$$\begin{cases} \Theta = C_c \Theta_0 \beta^{-0.257} \Psi^{-2.24} \; if \; p \leq 10 \text{ bar} \\ \Theta = C_c \Theta_0 \beta^{-0.540} \Psi^{-1.76} \; if \; p > 10 \text{ bar} \end{cases} \tag{B2}$$

For the current application, and given the fact that the outlet flow pressure must be low in cavitating conditions (low σ), the $p < 10$ bar correlation with $\Theta_0 = 6.51 \cdot 10^{-4}$ s is preferred, a correction factor $C_c = 13$ being applied as it has previously been advanced. The correlation is based on a corrected pressure difference Ψ, defined as:

$$\Psi = \left| \frac{p_V - p}{p_V} \right| \tag{B3}$$

where p_V and p must be expressed as absolute pressures. The equilibrium vapor mass fraction $\overline{Y}_{v,eq}$ is found from the Clausius-Clapeyron equation:

$$\overline{Y}_{V,eq} = \frac{h_L(p,T) - h_{L,sat}}{h_{V,sat} - h_{L,sat}} \tag{B4}$$

Where $h_L(p,T)$ is the liquid specific enthalpy at the working pressure p and temperature T, $h_{L,sat}$ is the specific enthalpy of the saturated liquid at the working temperature and $h_{V,sat}$ is the specific enthalpy of the saturated vapor at the working temperature. The magnitude of $\overline{Y}_{V,eq}$ is therefore bounded between 0 and 1, neglecting the subcooled and superheated regions as they are not relevant for phase change. In equation (B2), the vapor volume fraction β is used instead of the mass fraction or vapor quality Y_V. Hence, β can be trivially defined as:

$$\beta = \frac{\rho_L Y_V}{\rho_L Y_V + \rho_V (1 - Y_V)} \tag{B5}$$

In order to apply equation (B1), the Lagrangian time history of static pressure is required. However, the only information provided by the analytical solution is the spatial history (along x) of the velocity modulus. Hence, the static pressure coefficient C_p must be derived as a function of the non-dimensional horizontal coordinate in order to obtain the pressure history along the streamline.

$$C_p = \frac{p - p_{min}}{\frac{1}{2}\rho_L |\mathbf{V}_2|^2} = k^2 - \frac{|\mathbf{V}|^2}{|\mathbf{V}_2|^2} \tag{B6}$$

From the above definition, it is obvious that when $p_{min} = p_V$ the minimum value of $C_p = 0$ will be attained at the cavity interface, where $|\mathbf{V}| = k|\mathbf{V}_2|$. Then, once $|\mathbf{V}_2|$ has been computed as explained

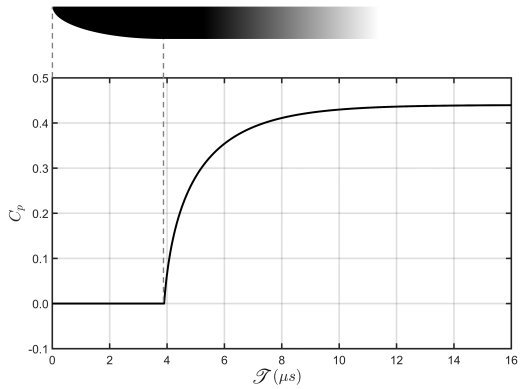

FIG. 21. Time evolution of the static pressure p along the free streamline for $\sigma = 0.44$, corresponding to $\Delta p = 7$ MPa in figure 20.

in Appendix A, the dimensional value of the static pressure p can be retrieved. In addition, the dimensional time along the streamline $\mathscr{T}$ can also be found applying the definition of velocity:

$$\frac{dx}{d\mathscr{T}} = \mathbf{V}_x(x) \rightarrow \mathscr{T} = \int_0^x \frac{dx}{V_x(x)} = \int_0^x \frac{dx}{|\mathbf{V}(x)|cos(\theta(x))} \tag{B7}$$

Using the above equations, the $C_p = f(\mathscr{T})$ distribution along the free streamline can be determined. As an example, this distribution is provided in figure 21 for $\sigma = 0.44$, corresponding to $\Delta p = 7$ MPa in figure 20. Pressure recovery after the cavity endpoint follows an asymptotic exponential law, as observed by Roshko[44] for the cavity behind a flat plate. Once the pressure profile along the streamline has been obtained, the vapor volume fraction is simply computed using second order backward differencing as:

$$Y_{V,\mathscr{T}} = \frac{4}{3}Y_{V,\mathscr{T}-1} - \frac{1}{3}Y_{V,\mathscr{T}-2} + \frac{2\Delta\mathscr{T}}{3}\frac{DY_V}{D\mathscr{T}} \tag{B8}$$

After $Y_{V,\mathscr{T}}$ is computed, the timescale $\mathscr{T}$ is converted back into space coordinates (x,y). The two-dimensional contours of void fraction are then calculated as a function of the vertical coordinate of the cavity interface $y_c(x)$:

$$Y_{V,\mathscr{T}}(x,y) = \begin{cases} 0 \; if \; y(x) \leq y_c(x) \\ \\ \frac{4}{3}Y_{V,\mathscr{T}-1}(x) - \frac{1}{3}Y_{V,\mathscr{T}-2}(x) + \\ \quad + \frac{2\Delta\mathscr{T}}{3}\frac{DY_V}{D\mathscr{T}} \end{cases} \quad if \; y(x) > y_c(x) \tag{B9}$$

Equation (B9) is used in figure 20 to represent the cavity morphology at the different values of Δp under analysis.

REFERENCES

[1]C. E. Brennen, *Cavitation and bubble dynamics* (Oxford University Press, 1995).
[2]J. Franc and J. Michel, *Fundamentals of Cavitation*, Vol. 76 (Springer Netherlands, 2005).
[3]C. E. Brennen, *Hydrodynamics of pumps* (Concepts ETI, 1994) p. 316.

[4]T. Melissaris, S. Schenke, and T. J. C. van Terwisga, "Cavitation erosion risk assessment for a marine propeller behind a ro–ro container vessel," Physics of Fluids **35** (2023), 10.1063/5.0131914.
[5]K. L. de Graaf, P. A. Brandner, and B. W. Pearce, "Spectral content of cloud cavitation about a sphere," Journal of Fluid Mechanics **812**, R1 (2017).
[6]C. Hu, Z. Wu, W. Huang, P. Leng, J. Deng, and L. Li, "Spray dynamics characteristics in gasoline direct injection injectors at varied orifice inlet angles," Physics of Fluids **37** (2025), 10.1063/5.0248414.
[7]K. A. Mørch, "Cavitation inception from bubble nuclei," (2015).
[8]X. Lyu, S. Pan, X. Hu, and N. A. Adams, "Numerical investigation of homogeneous cavitation nucleation in a microchannel," Physical Review Fluids **3**, 064303 (2018).
[9]L. Briançon-Marjollet, J. P. Franc, and J. M. Michel, "Transient bubbles interacting with an attached cavity and the boundary layer," Journal of Fluid Mechanics **218**, 355 (1990).
[10]J. A. Venning, B. W. Pearce, and P. A. Brandner, "Nucleation effects on cloud cavitation about a hydrofoil," Journal of Fluid Mechanics **947**, A1 (2022).
[11]P. A. Brandner, J. A. Venning, and B. W. Pearce, "Nucleation effects on cavitation about a sphere," Journal of Fluid Mechanics **946**, A1 (2022).
[12]C. Brennen, "A numerical solution of axisymmetric cavity flows," Journal of Fluid Mechanics **37**, 671–688 (1969).
[13]W. Bergwerk, "Flow pattern in diesel nozzle spray holes," Proceedings of the Institution of Mechanical Engineers **173**, 655–660 (1959).
[14]A. Sou, S. Hosokawa, and A. Tomiyama, "Effects of cavitation in a nozzle on liquid jet atomization," International Journal of Heat and Mass Transfer **50**, 3575–3582 (2007).
[15]Y. Yan and R. Thorpe, "Flow regime transitions due to cavitation in the flow through an orifice," International Journal of Multiphase Flow **16**, 1023–1045 (1990).
[16]L. He and F. Ruiz, "Effect of cavitation on flow and turbulence in plain orifices for high-speed atomization," Atomization and Sprays **5**, 569–584 (1995).
[17]M. Kato, H. Kano, K. Date, T. Oya, and K. Niizuma, "Flow analysis in nozzle hole in consideration of cavitation," (1997).
[18]I. K. Karathanassis, M. Heidari-Koochi, F. Koukouvinis, L. Weiss, P. Trtik, D. Spivey, M. Wensing, and M. Gavaises, "Quantification of cavitating flows with neutron imaging," Scientific Reports **14**, 26911 (2024).
[19]C. Wang and M. Zhang, "Dynamics of cavity structures and wall-pressure fluctuations associated with shedding mechanism in unsteady sheet/cloud cavitating flows," Flow **3**, E9 (2023).
[20]M. Özgünoğlu, G. Mouokue, M. Oevermann, and R. E. Bensow, "Numerical investigation of cavitation erosion in high-pressure fuel injector in the presence of surface deviations," Fuel **386**, 134174 (2025).
[21]Z. Wang, H. Cheng, and B. Ji, "Numerical prediction of cavitation erosion risk in an axisymmetric nozzle using a multi-scale approach," Physics of Fluids **34** (2022), 10.1063/5.0095833.
[22]B. A. Reid, M. Gavaises, N. Mitroglou, G. K. Hargrave, C. P. Garner, E. J. Long, and R. M. McDavid, "On the formation of string cavitation inside fuel injectors," Experiments in Fluids **55**, 1662 (2014).
[23]W. Guan, Y. Huang, Z. He, G. Guo, C. Wang, and D. Thévenin, "Primary breakup of a jet coupled with vortex-induced string cavitation in a fuel injector nozzle," Physics of Fluids **36** (2024), 10.1063/5.0204584.
[24]C. Li, Z. He, W. Guan, G. Guo, T. Bai, and B. Hu, "Investigations of string cavitation and air back suction during injection duration in the scaled-up diesel fuel injection nozzle," Fuel **339**, 126760 (2023).
[25]R. Susan-Resiga, G. D. Ciocan, I. Anton, and F. Avellan, "Analysis of the swirling flow downstream a francis turbine runner," Journal of Fluids Engineering **128**, 177–189 (2006).
[26]K. Im, S. Cheong, C. F. Powell, M. D. Lai, and J. Wang, "Unraveling the geometry dependence of in-nozzle cavitation in high-pressure injectors," Scientific Reports **3**, 2067 (2013).
[27]F. Salvador, D. Jaramillo, J.-V. Romero, and M.-D. Roselló, "Using a homogeneous equilibrium model for the study of the inner nozzle flow and cavitation pattern in convergent–divergent nozzles of diesel injectors," Journal of Computational and Applied Mathematics **309**, 630–641 (2017).
[28]T. S. Folden and F. J. Aschmoneit, "A classification and review of cavitation models with an emphasis on physical aspects of cavitation," Physics of Fluids **35** (2023), 10.1063/5.0157926.
[29]C. Hsiao, J. Ma, and G. L. Chahine, "Multiscale tow-phase flow modeling of sheet and cloud cavitation," International Journal of Multiphase Flow **90**, 102–117 (2017).
[30]A. Vallier, *Simulations of cavitation - from the large vapour structures to the small bubble dynamics* (Division of Fluid Mechanics, Department of Energy Sciences, Faculty of Engineering, Lund University, 2013).
[31]M. S. Plesset, "The dynamics of cavitation bubbles," Journal of Applied Mechanics **16**, 277–282 (1949).
[32]Y. Ye, C. Dong, Z. Zhang, and Y. Liang, "Modeling acoustic cavitation in homogeneous mixture framework," International Journal of Multiphase Flow **122**, 103142 (2020).
[33]J. Li and P. M. Carrica, "A population balance cavitation model," International Journal of Multiphase Flow **138**, 103617 (2021).
[34]L. Rayleigh, "On the pressure developed in a liquid during the collapse of a spherical cavity," The London, Edinburgh, and Dublin Philosophical Magazine and Journal of Science **34**, 94–98 (1917).
[35]J. Sauer, *Ein neues Modell, basierend auf Front Capturing (VoF) und Blasendynamik*, Ph.D. thesis (2000).
[36]R. Payri, F. Salvador, J. Gimeno, and J. de la Morena, "Study of cavitation phenomena based on a technique for visualizing bubbles in a liquid pressurized chamber," International Journal of Heat and Fluid Flow **30**, 768–777 (2009).
[37]R. B. Wade, "Linearized theory of a partially cavitating cascade of flat plate hydrofoils," Applied Scientific Research **17**, 169–188 (1967).
[38]C. E. Brennen, *Cavitation and other free surface phenomena*, Ph.D. thesis (1966).
[39]A. G. Terentiev, I. N. Kirschner, and J. S. Uhlman, *The hydrodynamics of cavitating flows* (Backbone Publishing Company, 2011).

[40]G. Birkhoff and E. H. Zarantonello, *Jets, wakes and cavities* (Academic Press, 1957).
[41]L. M. Milne-Thomson, *Theoretical Hydrodynamics*, 4th ed. (MacMillan and Co, 1962).
[42]M. S. Howe, "Ideal flow in two dimensions," in *Hydrodynamics and Sound* (Cambridge University Press, 2006) pp. 102–210.
[43]T. Y.-T. W. Wu and D. P. Wang, "A wake model for free-streamline flow theory part 2. cavity flows past obstacles of arbitrary profile," Journal of Fluid Mechanics **18**, 65–93 (1964).
[44]A. Roshko, "A new hodograph for free-streamline theory," (1954).
[45]N. Joukowsky, "Über die konturen der tragflächen der drachenflieger," Zeitschrift für Flugtechnik und Motorluftschiffahrt **1**, 281–284 (1910).
[46]E. Winklhofer, E. Kull, E. Kelz, and A. Morozov, "Comprehensive hydraulic and flow field documentation in model throttle experiments under cavitation conditions," in *ILASS Europe* (2001).
[47]R. Payri, J. Gimeno, P. Martí-Aldaraví, and M. Martínez, "Validation of a three-phase eulerian cfd model to account for cavitation and spray atomization phenomena," Journal of the Brazilian Society of Mechanical Sciences and Engineering **43**, 228 (2021).
[48]H. H. Ambrose, "Head losses in miter bends," in *Free-streamline analyses of transitional flow and jet deflection*, edited by J. S. McNoown and Y. Chia-Sun (University of Iowa, 1953) pp. 73–82.
[49]S. S. Chu, "Separated flow in bends of arbitrary turning angles, using the hodograph method and kirchhoff's free streamline theory," Journal of Fluids Engineering **125**, 438–442 (2003).
[50]R. R. Mankbadi and S. Zaki, "Computations of the contract coefficient of unsymmetrical bends," AIAA Journal **24**, 1285–1289 (1986).
[51]F. T. Smith and P. W. Duck, "On the severe non-symmetric constriction, curving or cornering of channel flows," Journal of Fluid Mechanics **98**, 727–753 (1980).
[52]D. P. Wang and T. Y.-T. Wu, "Small-time behavior of unsteady cavity flows," Archive for Rational Mechanics and Analysis **14**, 127–152 (1963).
[53]T. A. Driscoll, *Schwarz-Christoffel Mapping* (Cambridge University Press, 2002).
[54]P. K. Kythe, *Handbook of Conformal Mappings and Applications* (Chapman and Hall/CRC, 2019).
[55]F. M. White, "Viscous flow in ducts," in *Fluid Mechanics* (McGraw-Hill, 2011) pp. 347–456, 7th ed.
[56]Z. Bilicki and J. Kestin, "Physical aspects of the relaxation model in two-phase flow," Proceedings of the Royal Society of London. A. Mathematical and Physical Sciences **428**, 379–397 (1990).
[57]A. Einstein, "Schallausbreitung in teilweise dissoziierten gasen," Akademie der Wissenschaften , 379–403 (1920).
[58]P. Downar-Zapolski, Z. Bilicki, L. Bolle, and J. Franco, "The non-equilibrium relaxation model for one-dimensional flashing liquid flow," International Journal of Multiphase Flow **22**, 473–483 (1996).